Electronic Delivery Cover Sheet

INTERNATIONAL JOURNAL FOR NUMERICAL METHODS IN ENGINEERING
Int. J. Numer. Meth. Engng. **44**, 767–800 (1999)

THE ELEMENT FREE GALERKIN METHOD FOR DYNAMIC PROPAGATION OF ARBITRARY 3-D CRACKS

PETR KRYSL[†] AND TED BELYTSCHKO[*,‡]

Civil and Mechanical Engineering Departments, Northwestern University, Evanston, IL 60208, U.S.A.

SUMMARY

A technique for modelling of arbitrary three-dimensional dynamically propagating cracks in elastic bodies by the Element-Free Galerkin (EFG) method with explicit time integration is described. The meshless character of this approach expedites the description of the evolving discrete model; in contrast to the finite element method no remeshing of the domain is required. The crack surface is defined by a set of triangular elements. Techniques for updating the surface description are reported. The paper concludes with several examples: a simulation of mixed-mode growth of a center crack, mode-I surface-breaking penny-shaped crack, penny-shaped crack growing under mixed-mode conditions in a cube, and a bar with centre through crack.

KEY WORDS: three-dimensional crack growth; element-free Galerkin method; fracture; dynamic fracture

INTRODUCTION

Three-dimensional crack growth problems are of great interest in the simulation of failure. The three spatial dimensions make for large models, as compared to 2-D, and dynamic crack growth poses substantial additional difficulties. Two aspects of crack growth simulations are of interest: the mechanical (physical) model underlying the crack evolution, and the representation of an evolving geometry. The current computational technology for the modelling of stationary cracks is quite robust, but the representation of crack evolution of arbitrary three-dimensional cracks is still an embryonic field.

The main computational techniques currently used in fracture mechanics are the finite-difference method, the finite element method, and the boundary integral method. The suitability of these methods for simulation of arbitrary crack growth depends on the complexity of simulating the evolution of cracks with these discrete models, and the accuracy, versatility and speed of these methods. One of the most difficult aspects of modelling the evolution of cracks is the need to link an evolving solid model representation of the body to the discretization for each stage of the propagation. The ability of the so-called meshless methods[1] to minimize or simplify changes to the discrete model is why these methods are promising alternatives to the traditional approaches.

* Correspondence to: Ted Belytschko Departments of Civil and Mechanical Engineering, Northwestern University, Evanston, IL 60208, U.S.A. E-mail: t-belytschko@nwu.edu
† Research Assistant Professor
‡ Walter P. Murphy Professor of Mechanical Engineering

Contract/grant sponsor: Office of Naval Research

CCC 0029–5981/99/060767–34$17.50

Received 28 May 1997
Revised 26 May 1998

In this study, we explore the potential of the Element-Free Galerkin (EFG) method for simulating the evolution of arbitrary 3-D cracks in dynamic problems.

The outline of the paper is as follows. In Section 1 we discuss crack growth from the viewpoint of general simulation systems required for simulating the modelling components. We then review the existing literature from this vantage point. Next, we discuss the framework of the EFG method for crack growth problems, and to put things into perspective, we compare with the FEM or BEM as exemplified, for example, by the FRANC3D system,[2–6] to highlight both the advantages and the weak points of both methods. Section 2 describes the meshless discrete computational model, and the EFG superelement through which the EFG method is embedded in an explicit finite element system. Section 3 deals with construction of EFG shape functions. We present a consistent node inclusion criterion for the discontinuity surfaces (cracks), and discuss the impact of the discontinuities on the choice of the weight function. In Section 4, we deal with the implementation of the visibility criterion. Section 5 deals with the geometrical and topological management of the crack surface representation. A set of rules is proposed which allows for a variety of practically important situations, such as surface-breaking cracks, to be modelled.

The physical model for crack growth laws is almost distinct from the crack representation. The stress intensity factor-based model presented in Section 6 allows for a number of interesting problems to be modelled, and its implementation in the EFG setting is described. The stress intensity factors are extracted from interaction energy integrals in the domain (volume) form. The virtual extension domain is defined separately from the integration cells to allow for general crack front motion. A technique for the evaluation of these integrals, which is both relatively inexpensive and of adequate accuracy, is proposed.

The last section describes several numerical simulations: mixed mode growth of crack in a finite plate, mode-I surface-breaking penny-shaped crack, penny-shaped crack growing under mixed mode conditions in a cube, and crack growth under general mixed mode conditions in a bar under combined tension and torsion.

1. LITERATURE SURVEY

A key feature of crack growth simulation is the evolving geometry. The growth of the crack changes the computational model, and implementing these changes is one of the most difficult aspects of crack propagation simulations, particularly in three dimensions.

An analysis package for crack growth involves the components shown in Figure 1 (after Reference 7). For the ith step of crack growth, there are three data repositories: (1) R_i, is the representational database, which describes the problem; (2) the analysis database, A_i, which describes the computational model, tailored to the discretization method e.g. (FEM, BEM of EFG); it is generated from the representational database by the software component M (mesh generator). The generation may be as simple as adjustment of nodal release stiffness, or as complicated as a local remeshing of the domain (3) The variables representing the mechanical state of the body, such as the kinetic state E_i, the fracture parameters F_i. These parameters are computed by the solver S using the discrete model A_i.

The solution method S, to a considerable extent, determines the complexity of the other components. For example, in a finite element solver using remeshing after each crack motion, the constraints on the quality of the mesh around the crack front can be severe. On the other hand,

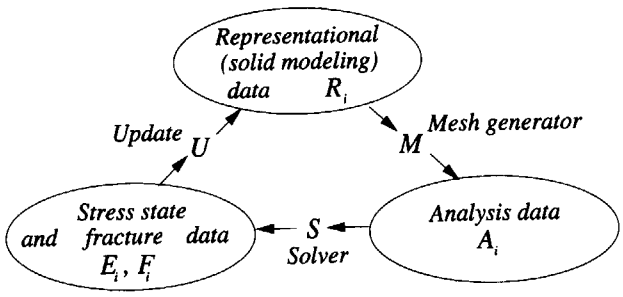

Figure 1. Databases and transformation functions of a topology-based crack propagation system

the boundary element method poses lesser demands on the meshing component M, because only a surface mesh is needed.

The cycle of Figure 1 is closed by the update function U, which computes the shape of the crack for the step $i + 1$. The update may amount to no more than a new location of the crack tip (e.g. in the moving mesh technique in 2-D), or it may involve changes in the solid model database affected by a complicated suite of update operators.

The diagram of Figure 1 is quite general, and neither the databases nor the transformation operators always appear in the simulation system explicitly. The effectiveness of crack growth simulation systems will depend on the complexity of the required databases and on the efficiency with which the databases can be updated during crack evolution. The choice of the solver effects both the discretization (volume meshes are more complicated to generate than surface meshes), and the representation database.

1.1. 2-D crack growth simulations

There is a substantial body of literature concerned with the simulation of two-dimensional crack growth; see, for instance, the review article by Nishioka.[8] One of the most often used approaches is the nodal release technique; see, e.g., Chen and Wilkins[9] using a finite-difference technique *et al.*,[10] who used FEM, and Ivankovic and Williams[11] using a finite volume method. The major disadvantage of the nodal release approach is that the path of the crack is limited to the mesh edges.

The moving mesh technique was used by Atluri and Nishioka[12] (with the FEM), Koh, Lee and Haber[13] (Eulerian–Lagrangian description in conjunction with the FEM), Gallego and Dominguez[14] (BEM with a moving singular element), Koh *et al.*,[15] (Eulerian–Lagrangian description in conjunction with the FEM). Modelling arbitrary curved crack growth seems to be difficult with this approach, since excessive mesh distortion will occur.

Boundary integral methods or the FEM are applicable to arbitrary mixed-mode cracks when combined with a remeshing of the discrete model after each crack increment. Automatic remeshing has been used, e.g. by Swenson and Ingraffea[16] and Bittencourt *et al.*,[17] in the framework of the FRANC2D system. Xie *et al.*[18] and Xie and Gerstle[19] describe a 2-D system using singular finite elements with a virtual crack extension and special remeshing rules. Portela *et al.*[20] report an application of the dual boundary element method to crack propagation.

While the remeshing technique allows for an arbitrary path, it also has certain disadvantages. It is highly desirable, especially in 3-D, to free the analyst of repeated interventions in the remeshing. In order to achieve this goal, the update function U and the mesh generator M need to operate on their

respective databases automatically. However, the complexity of these operations is considerable, especially in three dimensions, and the associated cost in terms of implementation effort can be very high.

Several reports on the use of the element-free Galerkin method in arbitrary crack propagation have appeared: References 1, 21–29. All of these deal with two-dimensional fracture. Nevertheless, certain features which make the EFG method appealing for arbitrary three-dimensional discrete cracks are already apparent in 2-D EFG simulations: the arbitrariness of the crack path, the high-order character of the trial functions, the ability to use a time-invariant integration cell structure, and the relaxed compatibility requirements between the crack discretization and the cell structure. The enhancement of the trial space by the asymptotic fields, which proved extremely useful in 2-D EFG simulations, is currently under investigation also in the three-dimensional setting; see Sukumar *et al.*[30]

1.2. 3-D crack growth simulations

The following overview of the literature on three-dimensional crack growth simulations, while not complete, documents various aspects of the subject.

A system for crack propagation based on general solid modelling, analysis and fracture components was described by Gerstle *et al.*[31,32] The crack was evolved essentially manually. Martha[2] and Martha *et al.*[3] report a more advanced system, the integrated environment FRANC3D, which allows for a semi-automatic treatment of general three-dimensional cracks. Germanovich, Carter, Ingraffea, Dyskin and Lee[33] describe application of the FRANC3D system to the growth of multiple cracks under compression.

Bower and Ortiz[34] describe analysis of a crack which propagates through tougher particles. Xu and Ortiz[35] apply a boundary integral equation to the propagation of a planar crack, and Xu *et al.*[36] report a technique which allows propagation of a planar or almost planar crack under mixed mode conditions. The crack is allowed to assume a wavy shape, which is excited by the tearing mode of loading. A boundary integral approach is adopted, which requires only the crack to be discretized and remeshed at successive stages of its evolution. Ortiz[37] describes a simulation of crack propagation through an array of bridging fibers. The originally planar crack is allowed to follow the surfaces of the fibers, resulting in a truly three-dimensional approach. Only the crack surface needs to be discretized due to the use of a boundary integral equation formulation. Mi and Aliabadi[38] describe an application of a dual boundary element method to quasistatic and fatigue 3-D crack propagation. The discrete model is apparently updated manually after each increment.

Červenka[39] describes the MERLIN system for 3-D fracture simulation. The composition of the system follows the general rules outlined in Figure 1, with a boundary representation of the cracked structure, FE mesh generator and FE solver. The update of the boundary representation is manual. Geubelle and Rice[40] proposed a spectral technique for elastodynamics of planar cracks, and applied the approach to the propagation of a crack through a row of circular asperities.

Wawrzynek *et al.*[7] propose a fracture simulation system in the form depicted in Figure 1. The system is equipped with a built-in solid modelling system, mesh generators and fracture prediction component. Potyondy *et al.*[4] report an application of the FRANC3D system in simulations of fractures in aircraft. Carter *et al.*[41] and Carter *et al.*,[6] and Desroches and Carter[5] describe new capabilities in the FRANC3D system, allowing for an automatic treatment of multiple, non-planar, surface, internal and surface-breaking cracks, in or across material interfaces, and intersecting cracks.

Galdos[42] has applied the FEM to the propagation of planar cracks. The FE mesh is regenerated after a crack increment through a solution of a Laplace equation designed to produce gradual transition between successive meshes. The technique is applicable only to a succession of meshes with the same connectivity (topology).

2. DISCRETE EFG MODEL

2.1. Main assumptions

In this paper, we adopt the physical model of Linear Elastic Fracture Mechanics (LEFM) in a dynamic setting. The representational model of crack growth can be treated to a considerable extent separately from the physical model. The physical and the representational models described here can treat multiple, non-interacting cracks. We do not model branching of the crack surface. While the representational model could be extended to handle interacting fronts, branching surfaces, and corners, the physical model is not so easily extended for these capabilities.

The present framework allows for internal or surface-breaking cracks. However, the crack evolution laws available in the literature do not apply in general to arbitrarily propagating surface cracks, so the approach presented here is a rough model synthesized from what is available.

The numerical model consists of a set of nodes, a representation of external surfaces and a representation of the crack. The crack is represented by triangular 3-node elements which provide a piecewise linear representation of the crack surface, see Figure 2. The external surfaces are represented by a union of patches which enclose the volume. The patches may be curved, but in most cases planar patches are used.

2.2. EFG shape functions

The approximation is constructed by the Element-Free Galerkin (EFG) method.[54] The shape functions in the EFG method are constructed by the moving least-squares technique, or alternatively on the basis of reproducibility conditions. Both approaches arrive at the same expressions for the shape function. The moving least-squares technique can be traced to scattered data fitting, where it has been studied under different names (local regression, 'loess', and moving least-squares) since the 1920s; cf. References 43 and 44. The use of reproducibility conditions to modify the weight function to produce a shape function was described by Belytschko *et al.*[45] and Liu *et al.*[46] The EFG shape functions in the present work are evaluated using the ESFLIB library, described by Krysl and Belytschko.[47]

To make the paper self-contained, we present a brief account of the moving least square approximation functions. Each EFG node is associated with a positive weight function of compact support. The support of the weight function defines the domain of influence of the node; the shape function associated with the node assumes non-zero values in the domain of influence. In mathematical terms, the domain of influence of node I is given by

$$B_I = \{\mathbf{x} \in R^3 \colon w_I(\mathbf{x}) = w(\mathbf{x}, \mathbf{x}_I) > 0\} \tag{1}$$

The approximation at a point $\hat{\mathbf{x}}$ is affected by only those nodes whose weights are non-zero at that point. We call the set of such nodes the *active set*, $\mathscr{A}(\hat{\mathbf{x}})$.

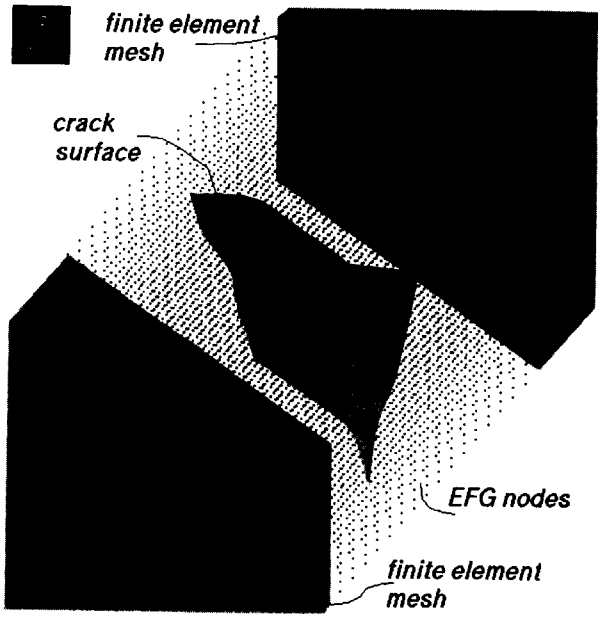

Figure 2. Through-crack under combined torsion and tension. The discretization

The approximation to a function $u(\mathbf{x},t)$ in Ω is

$$u(\mathbf{x}) \approx u_h(\mathbf{x},t) = \sum_{I \in \mathscr{A}(\mathbf{x})} \phi_I(\mathbf{x}) u_I(t) = \sum_{I \in \mathscr{A}(\mathbf{x})} \mathbf{a}(\mathbf{x},t)^{\mathrm{T}} \mathbf{g}(\mathbf{x}) w(\mathbf{x},\mathbf{x}_I) \tag{2}$$

where $\mathbf{g}(\mathbf{x})$ is a column matrix of the linear basis in a 3-D space: $\mathbf{g}(\mathbf{x}) = \{1, x, y, z\}^{\mathrm{T}}$; u_I are coefficients (nodal unknowns). Note that the nodal coefficients are not necessarily the values of the function u at the nodes, $u(\mathbf{x}_I) \neq u_I$. The weight functions are time dependent in the vicinity of the crack path, but we neglect this time dependence.

The coefficients $\mathbf{a}(\mathbf{x},t)$ are obtained by minimizing a weighted least square form,[21] yielding the linear equations

$$\mathbf{A}(\mathbf{x})\mathbf{a}(\mathbf{x},t) = \mathbf{g}(\mathbf{x}) \tag{3}$$

where $\mathbf{A}$ is given by

$$A_{ij} = \sum_{I \in \mathscr{A}(\mathbf{x})} w(\mathbf{x}_I,t) g_i(\mathbf{x}_I) g_j(\mathbf{x}_I) \tag{4}$$

The matrix $\mathbf{A}$ is symmetric. Under certain conditions it is positive-definite,[47] and is often called the moment matrix. The matrix $\mathbf{A}$ is usually factorized by pivoting LU factorization, QR or singular value decomposition (the latter two are indicated for ill-conditioned matrices).

The spatial derivatives of the shape functions are obtained by noting that the differentiation of (3) yields[48]

$$\mathbf{A}_{,i}\mathbf{a} + \mathbf{A}\mathbf{a}_{,i} = \mathbf{g}_{,i} \tag{5}$$

where $\mathbf{g}_{,i}$ denotes $\partial \mathbf{g}/\partial x_i$. Thus, we can obtain the derivatives of $\mathbf{a}_{,i}$ by solving

$$\mathbf{A}\mathbf{a}_{,i} = \mathbf{g}_{,i} - \mathbf{A}_{,i}\mathbf{a} \tag{6}$$

For this purpose, the factorization of $\mathbf{A}$ in (3) can be reused, so the computation of the derivatives involves little extra effort.

2.3. *Weight function*

We have used truncated Gaussian weight functions on spherical supports. In crack problems, we have obtained consistently better results with the discontinuous shape functions which result from the visibility criterion (see Sections 3 and 4) and the truncated Gaussian weight function:

$$w(\mathbf{x}_I, \mathbf{x}) = w(r) = \frac{\exp(-\beta^2 r^2) - \exp(-\beta^2)}{1 - \exp(-\beta^2)} \tag{7}$$

In the above expression, $r = \|\mathbf{x}_I - \mathbf{x}\|/d_{mI}$, with d_{mI} being the radius of the spherical support. The parameter β governs the shape of the weight function bell, we have used $\beta = 4$.

The reasons for the better performance of the truncated Gaussian weight function when combined with the discontinuous shape functions seem to be due to the interplay of the weight function and of the interior discontinuities arising from the crack when the visibility criterion is used; see Section 3. We have noticed in our numerical experiments that the stress intensity factors converge from above for the discontinuous approximation, since this leads to a non-conforming approximation.[49] This is not unexpected since non-conforming approximations relax the constraints. One can infer intuitively that as the jumps in the shape functions decrease, the loss of compatibility becomes less pronounced. The jumps in the shape functions depend on jumps in the weight functions. The parameter β makes it possible to change the shape of the truncated Gaussian weight, so it is narrower, or, in other words, to increase its decay towards the circumference. (This is not possible with the polynomial weight functions.) Faster decay decreases the discontinuities. This could be one reason for the improved performance of the Gaussian weight functions with discontinuous approximations.

The discrete equations are obtained from the standard Galerkin weak form of the momentum equation

$$\int_\Omega \rho \Phi_I \Phi_J \, \mathrm{d}\Omega \dot{v}_{iJ} + \int_\Omega \frac{\partial \Phi_I}{\partial x_j} \sigma_{ji} \, \mathrm{d}\Omega - \int_{\Gamma_t} \Phi_I t_i \, \mathrm{d}\Gamma = 0 \tag{8}$$

where ρ is the density, σ_{ji} the stress and t_i the applied traction. The mass matrix resulting from the first integral in the above is diagonalized by the row-sum technique. The mass matrix in the vicinity of the crack front needs to be updated as the crack progresses since the shape functions change due to the change of the domains of influence of the nodes.

2.4. *EFG superelement*

The EFG method is inherently more expensive (per degree of freedom) than the FE method. When modelling cracks, the flexibility of the EFG method is typically needed only in a restricted volume, i.e. close to the expected path of the crack; the rest of the domain can be modelled

conveniently by finite elements. For situations where nothing is known about the crack path in advance, the EFG subdomain can be generated adaptively.

We use the blending (coupling) technique to construct the approximating space on the domain.[50, 51, 47] This allows us to discretize with finite elements, and treat a subdomain as an EFG superelement; see Reference 52 for details. This technique not only contributes to the economy of the computation, but also permits convenient enforcement of the essential boundary conditions. The EFG shape functions are modified to be identical to the FE shape functions near the interfaces with finite elements; see Reference 47. The EFG superelement makes use of two types of nodes: internal nodes, which are associated with internal degrees of freedom, and the nodes at the interfaces of the EFG superelement with the rest of the FE domain, which are just aliases for the global FE nodes. The EFG superelement is integrated seamlessly with the finite element system, including parallelization (see Reference 53).

2.5. *Volume quadrature*

The present work uses hexahedral FE meshes as the initial discretization of the domain. The volume of the EFG superelement is also subdivided into hexahedral cells, which are called *background cells*.[54]

In the initial model, the nodes are placed at the vertices of the background cells. They could be also placed anywhere else, e.g. at the centres of the background cells. Our numerical experiments suggest that the difference is not important. The integration is performed on the background cells by Gaussian quadrature. Quadrature in EFG is at present not well understood. The two usual objectives, accuracy and cost, conflict to a certain extent. Drawing from our experience, we have

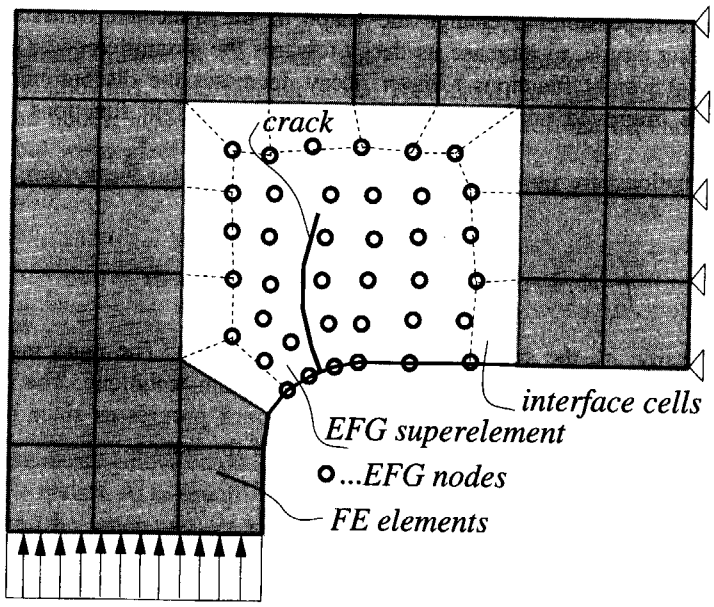

Figure 3. Coupled FE/EFG discretization

chosen $2 \times 2 \times 2$ quadrature. Since the EFG shape functions are non-polynomial, we do not use a high-order rule, but when necessary we subdivide the background cells into smaller ones. The subdivision of a cell is a very simple operation, because the refinement of a cell is completely independent of adjacent cells (see Figure 3).

2.6. *Boundary description*

The description of the external and internal boundaries, i.e. cracks, of the body finds twofold use in the present approach. First, the crack surface is essential in the modelling of the displacement discontinuity. Second, the external boundary limits the motion of the crack surface during its growth. The crack faces are described in the form of a triangulation. The roles played by the external surfaces are discussed in Section 4.

2.7. *Time integration*

The explicit version of the Newmark algorithm[55] is used. In each step we perform a series of actions such as the time step change, output, graphics update, and propagation of the crack surfaces.

3. EFG SHAPE FUNCTIONS ON NON-CONVEX DOMAINS

Crack surfaces and corners of the domain require a modification of the domains of influence of the nodes, i.e. the weight function, in their vicinity because they introduce discontinuities in the displacements fields. Let the surface of discontinuity, such as a crack, be Γ and the domain of influence (support) of node I be B_I.

The first step in the treatment of discontinuities is to decide whether a node should be included in the active set $\mathscr{A}(\hat{\mathbf{x}})$ (described in Section 2) of a given point $\hat{\mathbf{x}}$. Reference 49 lists two criteria: According to the *visibility criterion*, (see Section 3), if the unmodified domain of influence of the node I covers the point $\hat{\mathbf{x}}$, node I is included in the active set $\mathscr{A}(\hat{\mathbf{x}})$ if node I is visible from the point $\hat{\mathbf{x}}$ with the discontinuity surface considered to be 'opaque'. In the *contained-path criterion*, node I is included in the set $\mathscr{A}(\hat{\mathbf{x}})$ if node I can be reached from $\hat{\mathbf{x}}$ by a path C without leaving the intersection of Ω and B_I, and without crossing the discontinuity Γ.

When the visibility criterion is used, the domains of influence are truncated by the exclusion of the 'shadows' and the resulting shape functions are discontinuous along rays emanating from the crack tip. However, as shown in Reference 49, the EFG approximation is still convergent; the discontinuous approximations give very good results, often better than the continuous approximations with a linear basis.

3.1. *Implementation of the node inclusion criteria*

The node inclusion/exclusion is decided by ESFLIB using the algorithm summarized in Figure 4. The following comments regarding the algorithm of Figure 4 apply:

(1) The 'node qualifies by weight?' predicate is expressed simply as $w_I(\mathbf{x})>0$, where $w_I(\mathbf{x})$ is the value of the weight function associated with node I at point $\mathbf{x}$.

```
if "node qualifies by weight?" or "node is at interface cell vertex?"
    if "node is at interface cell vertex?"
        include node in the active set
    else
        if "procedure to check for exclusion by boundary defined?"
            if not "excluded by boundary?"
                include node in the active set
            endif
        else
            include node in the active set
        endif
    endif
endif
```

Figure 4. Check for inclusion of a node in the active set

(2) If the shape functions are evaluated inside a blending region, the predicate 'node is at interface cell vertex?' evaluates to TRUE if the node I is located at one of the vertices of the blending region; otherwise, it evaluates to FALSE.
(3) The predicate 'excluded by boundary?' is the value returned by the function checking for exclusion by the boundary (cracks). Either of the above criteria apply.

4. IMPLEMENTATION OF THE VISIBILITY CRITERION

While the visibility criterion is apparently simple, we have encountered difficulties in implementation related to degenerate positions of the line segments and triangles. To illustrate the difficulties, let us consider the situation depicted in Figure 5. Note that nodes I and K lie *on* the external boundary surface. If one postulates that the external surface is opaque, then according to the visibility criterion, node I should not be included in the active set of point $\mathbf{x}$. On the other hand, when performing the visibility check for the node K, the result will depend on round-off; node K can be determined to be either outside, inside or on the boundary depending on the round-off error.In Figure 6, nodes I, J and K are located on the boundary. Both I and J should be members of the active set $\mathscr{A}(\mathbf{x}_K)$. However, either of the nodes can be excluded when finite precision arithmetic indicates that the segment $\mathbf{x}_K\mathbf{x}$ intersects part of the boundary.

Another, ambiguous situation occurs when a point is located on an opaque surface such as a crack, as shown in Figure 7. Depending on the precision of the arithmetic operations, the nodes located directly on the crack surface are assigned to active sets of points on either side of the crack. Note that we cannot avoid points which are located on an opaque surface, since the points we are dealing with are quadrature points, nodes, vertices of the background mesh and vertices of the boundary patches. While the first two types of points are related to the Galerkin procedure, the latter describe the discontinuity surface and are used in post-processing. These problems in the intersection test could be resolved by introducing a topological model in which all points are classified with respect to the bounding surfaces and interiors. However, that is precisely what we wish to avoid, due to the associated complexity and cost. We have resolved the difficulty by treating the bounding surfaces as three-dimensional bodies, i.e. surfaces with a non-zero thickness.

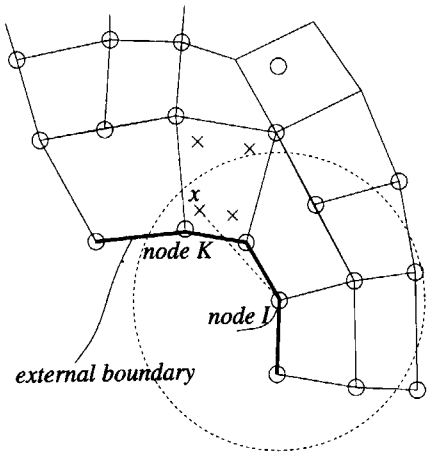

Figure 5. Evaluating the shape functions near a concave boundary. Node I lies on the boundary

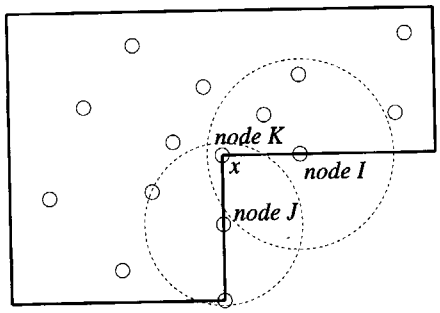

Figure 6. Evaluating the shape functions near a concave boundary. Nodes I, J and K lie on the boundary

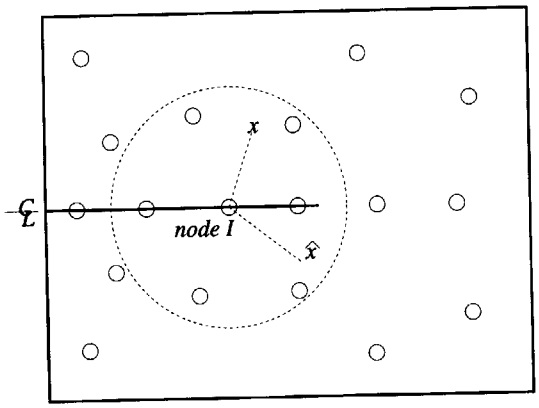

Figure 7. Evaluating the shape functions near the crack surface. Node I is located on the crack surface

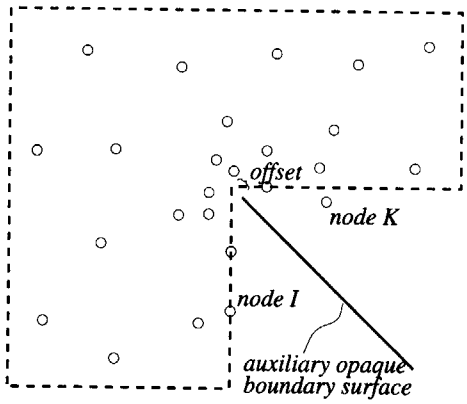

Figure 8. Use of an auxiliary opaque surface to enforce a concave corner. Node I is located on the surface of the domain, node K is located outside of domain

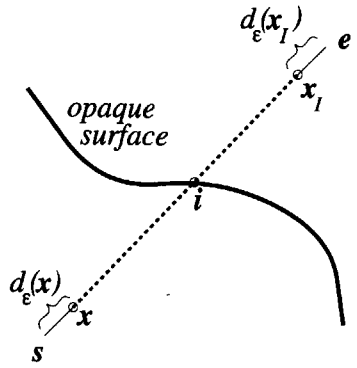

Figure 9. Extended segment connecting the evaluation point $\mathbf{x}$ and the location of the node I, $\mathbf{x}_I$

We consider only true crack surfaces in the visibility checks; all other external bounding surfaces are assumed transparent, and therefore are ignored in visibility checks (for external boundaries in which it is desirable to truncate domains of influence, for example a reentrant corner, an auxiliary opaque surface can be used as shown in Figure 8. The 'solid' model of the crack is achieved by creating a halo or envelope around the surfaces. Points are classified as being *on* the crack surface if they are found to be located inside the halo of the crack surface.

In the test an adjustment is made of the segment tested. Consider the end-points of a straight-line segment connecting the evaluation point and a node. The segment is extended as illustrated in Figure 9. The original segment $\overline{\mathbf{x}\mathbf{x}_I}$ is replaced by the segment $\overline{\mathbf{s}\mathbf{e}}$, with end-points $\mathbf{s}$ and $\mathbf{e}$ displaced from the original end-points by small distances, $d_\varepsilon(\mathbf{x})$ and $d_\varepsilon(\mathbf{x}_I)$ along the connecting line.

When the visibility criterion is applied, the intersection denoted by $\mathbf{i}$ of the extended segment with the crack surface is computed. If the distance between the intersection point $\mathbf{i}$ and the point $\mathbf{x}$ or $\mathbf{x}_I$, $d = \|\mathbf{x} - \mathbf{i}\|$, and $d = \|\mathbf{x}_I - \mathbf{i}\|$, respectively, is less than the tolerance $d_\varepsilon(\mathbf{x})$: $d < d_\varepsilon(\mathbf{x})$, the point $\mathbf{x}$ or $\mathbf{x}_I$ is classified as being located on the crack surface. The point or node $\mathbf{x}_I$ is then split into two points which are moved outside the halo.

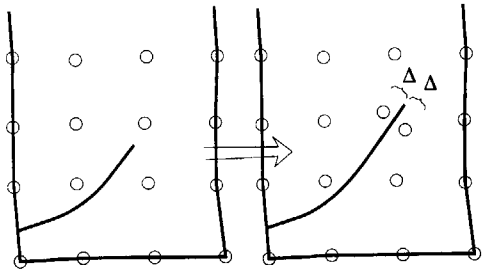

Figure 10. Splitting of a node located in the path of the crack

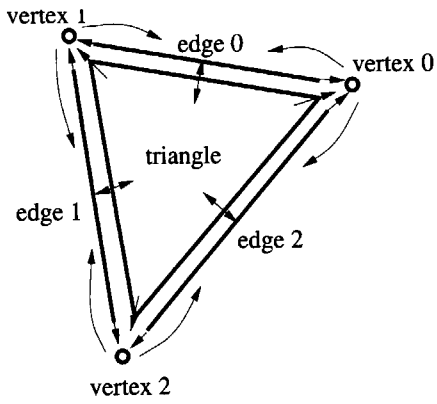

Figure 11. Topological information maintained for the crack surface entities

Nodes seldom appear in the halo, because we check for nodes in the path of the crack. If there are any, we split them and move them sufficiently far away from the anticipated crack path as illustrated in Figure 10; see also Reference 56. After the split, the state variables are associated with the same kinematic quantities, but with a portion of the mass.

5. REPRESENTATION OF THE CRACK SURFACE

The crack surface is represented by a collection of flat triangles, and the crack front consists of straight-line segments. A smooth representation is not used because there may be kinks and creases in the crack surface, which would have to be identified as features in a smooth crack model.

The triangulation of the crack is kept topologically consistent during the crack evolution to allow for efficient and accurate adjacency and geometry queries. Thus, each entity (vertex, edge, triangle) refers to a number of other entities through references, which in Figure 11 are represented by arrows. In addition to the topology information, a vertex carries flags that indicate whether it is located on the crack front, whether it is bound to an exterior surface of the body, etc.

```
algorithm PROPAGATE
do
    if crack is stationary return
    foreach crack front vertex /* (i) */
        compute SIF's in a local coordinate system
    endforeach
    foreach crack front vertex /* (ii) */
        advance vertex
    endforeach
    foreach crack front vertex bound to boundary /* (iii) */
        trim edge
    endforeach
    foreach crack front vertex /* (iv) */
        adjust vertex status
    endforeach
    foreach crack front edge /* (v) */
        adaptively adjust front subdivision
    endforeach
enddo
```

Figure 12. Algorithm of crack propagation

5.1. *Crack propagation algorithm*

The crack propagation algorithm is summarized in Figure 12.

1. The stress intensity factors at the crack front are used to drive the advance of the crack; we call the advance at a vertex an advance vector. The advance vector generate new vertices, from which additional triangular elements and crack edges are generated.
2. The locations of the new vertices which are adjacent to exterior surfaces are adjusted by trimming the advance vectors. In preparation for trimming, the advance vectors of vertices which are already on exterior surfaces are projected onto the exterior surface. Then, for each vertex on the crack front, if its advance vector intersects an exterior surface patch, it is trimmed by the surface and the vertex is marked as bound to the boundary patch. The algorithm allows vertices to pass around corners in the surface of the body; see Figure 13, where the vertex at the left boundary surface follows the vertical part of the boundary until the corner is reached, then it follows the horizontal surface and continues to the right.
3. For each vertex on an exterior surface, the edge emanating from it is trimmed by the exterior surfaces. This means it is either cut or extended to the intersection of the edge with the boundary. The reason for this operation is that the boundary faces are not necessarily planar, so the projection of the advance vector may not yield a point on the boundary surface.
4. The status of the vertices on the front is updated to determine whether a crack can advance. Subsequently, if a vertex is bound to a boundary patch, the crack can advance at the vertex only if it is connected by an edge to an unbound vertex. If a vertex is bound to the boundary, and both edges emanating from it are bound to the boundary, the crack cannot advance at this vertex.

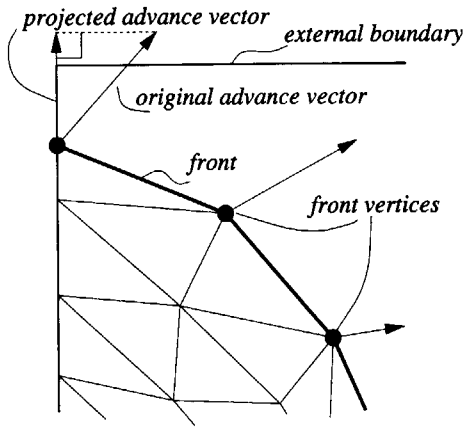

Figure 13. Modification of the advance vector when the front moves through a convex corner of the domain

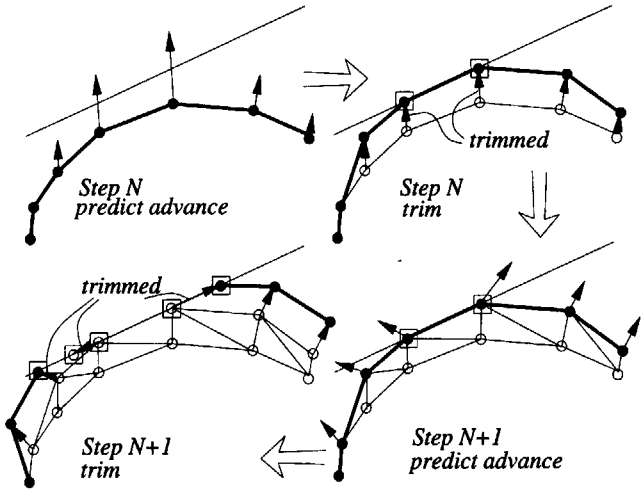

Figure 14. Two steps of crack propagation. Only the operations of advance prediction and trimming are shown

The procedures described above are illustrated in Figure 14, which shows the advance of a crack front through two crack steps. The solid circle (•) denotes a vertex which is completely free. Vertices denoted by a square box (□) are constrained to stay on the exterior surface. An empty circle inside a box denotes a vertex on the crack surface which can no longer move.

5.2. *Adaptive front discretization*

The crack front edges can become too long or too short in some cases. Since the domains for stress intensity factor evaluation are set up to correspond to crack front edge lengths, it is desirable

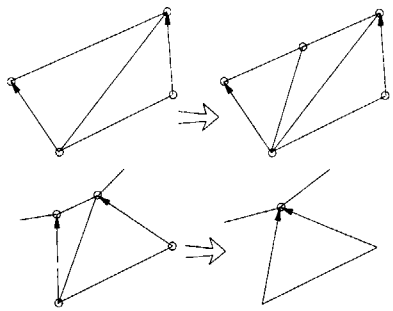

Figure 15. Adaptive discretization of the crack front to avoid excessively long or short edges

to avoid this. A simple adaptive approach is illustrated in Figure 15. Excessively long edges are subdivided into two shorter ones, and edges which are too short are deleted.

5.3. *Recomputation of shape functions*

If any part of the crack surface has advanced, the shape functions in its vicinity need to be updated. In order to recompute the shape functions selectively, we maintain a time stamp for background cells, the EFG superelement and for the shape functions. A set of rectangular 3-D boxes whose union defines the *region of invalidated connectivities* (RIC) is defined. When a crack advances, i.e. when a new triangle is added to a crack surface, we add a box to the RIC corresponding to the bounding box of the triangle, inflated by the largest support size.

When some connectivities have been invalidated by a crack advance, each shape function that may be effected is checked to see if it needs updating. This check is made as follows: at each quadrature point inside the RIC, rays $\overline{\mathbf{x}\mathbf{x}_I}$ for each node I are checked for intersection with the new triangles. If any ray was severed, the shape function is re-evaluated at that point. This strategy is designed to take advantage of the fact that the number of new triangles in the crack surface representation is considerably lower than the total number of triangles in the current crack, and avoids the time-consuming task of cheking all points against all crack surface elements in every time step.

6. PHYSICAL CRACK PROPAGATION MODEL

6.1. *Physical model*

The crack growth model is based on energy release rates. We estimate the dynamic energy release rate of a moving crack $G(C)$ from the energy release rate for a stationary crack $G(0)$.[57]

$$G(C) = \left(1 - \frac{C}{C_R}\right) G(0) \tag{9}$$

where C is the crack front speed and C_R is the Rayleigh wave speed, given as a root of the equation $D(C)=4\beta_1\beta_2-(1+\beta_2^2)^2=0$, where $\beta_1^2=1-(C/c_d)^2$, and $\beta_2^2=1-(C/c_s)^2$, with c_s the shear wave speed, and c_d the dilatational wave speed.

The crack speed is given by the following:

$$C=\begin{cases}0 & \text{for } G(C)<G_{crit}(0)\\ C_R\left(1-\frac{G_{crit}(C)}{G(C)}\right) & \text{otherwise}\end{cases} \tag{10}$$

The critical energy release rate depends on the dynamic fracture toughness for a mode-I crack:

$$G_{crit}(C)=\frac{K_{ID}^2(C)}{E^*} \tag{11}$$

where E^* is the effective Young's modulus proposed by Cherapanov:[64]

$$E^*=E\left[\frac{1}{1-\nu^2}+\frac{\nu}{1+\nu}\frac{\varepsilon_t}{\varepsilon_n+\varepsilon_f}\right] \tag{12}$$

where ε_t, ε_n, and ε_f are strains measured close to the crack front along the tangent, normal, and binormal to the crack front (surface). The dynamic fracture toughness is a function of the crack speed given by

$$K_{ID}(C)=\begin{cases}K_{IC} & \text{for } C=0\\ K_{IA}\left[1-\left(\frac{C}{C_R}\right)^m\right]^{-1} & \text{for } C>0\end{cases} \tag{13}$$

In the above, K_{IC} is the fracture initiation toughness,[58] K_{IA} is the fracture arrest toughness.

Equations (9) and (10) with (13) yield a non-linear equation for the crack speed C. For the simplest case of crack-speed independent fracture toughness, $K_{ID}(C)=\hat{K}_{ID}$, the crack speed is obtained from a quadratic equation.

6.2. *Crack extension*

Let $\hat{\mathbf{e}}_2$ be the normal to the crack surface, $\hat{\mathbf{e}}_3$ the tangent to the crack front, and $\hat{\mathbf{e}}_1$ the binormal. Figure 16 shows these vectors for a continuously differentiable crack front. At the vertices on the crack front in the plane $\mathbf{O}\hat{\mathbf{e}}_1\hat{\mathbf{e}}_2$, the crack surface and crack front are not differentiable, since the crack surface is piecewise linear. The normal and binormal are therefore obtained by averaging

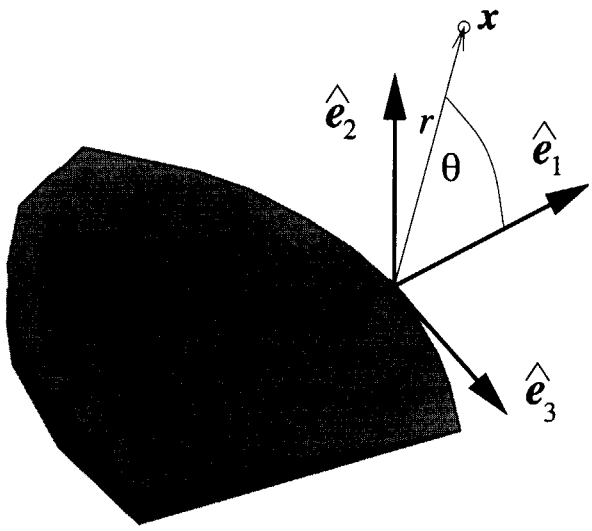

Figure 16. Local co-ordinate system at the crack front

the weighted normals of the triangular areas and crack front segments by

$$\hat{\mathbf{e}}_1 = \frac{\sum_i \hat{\mathbf{e}}_1^i l_i}{\sum_i l_i} \tag{14}$$

$$\hat{\mathbf{e}}_2 = \frac{\sum_i \hat{\mathbf{e}}_2^i A_i}{\sum_i A_i} \tag{15}$$

where A_i are the areas of the triangular elements connected to the vertex and l_i are the lengths of the line segments connected to the vertex; since $\hat{\mathbf{e}}_1$ computed by the above is not orthogonal to $\hat{\mathbf{e}}_2$, the projection of $\hat{\mathbf{e}}_1$ on $\hat{\mathbf{e}}_2$ is removed and $\hat{\mathbf{e}}_1$ is renormalized. The tangent vector $\hat{\mathbf{e}}_3$ is computed by $\hat{\mathbf{e}}_3 = \hat{\mathbf{e}}_1 \times \hat{\mathbf{e}}_2$.

Two-dimensional cracks extend in brittle materials so that the shearing (mode II) stress intensity factor (SIF) K_{II} is minimized.[59] All the criteria (maximum circumferential tensile stress,[60] maximum energy release rate,[61] critical strain energy density[62]) commonly adopted in fracture mechanics give similar results for relatively small ratios of $K_{\mathrm{II}}/K_{\mathrm{I}}$. However, in three-dimensional situations, the tearing mode may become important. There is no consensus yet on how the crack extends for a general 3-D mixed-mode situation, mainly because the relationship between the tearing mode and the tendency of the crack front to twist is not known. To simplify matters, we assume that only modes I and II affect the direction of the crack; mode III is assumed not to affect the direction of crack growth, only its speed.

The direction of motion of the vertices is based on the maximal circumferential tensile stress criterion[60] according to which the angle θ with respect to the plane $\mathbf{O}\hat{\mathbf{e}}_1\hat{\mathbf{e}}_2$ (see Figure 16) of the crack advance is given by

$$\theta = 2\arctan\tfrac{1}{4}(K_{\mathrm{I}}/K_{\mathrm{II}} \pm \sqrt{(K_{\mathrm{I}}/K_{\mathrm{II}})^2 + 8}) \tag{16}$$

where the SIFs are evaluated in the local-coordinate system at the crack front as defined in Figure 16. The sign in equation (16) is chosen to correspond to an opening (positive) mode I stress intensity factor for the direction given by θ.

Substituting the angle θ into the appropriate expression for the mode I stress intensity factor, we arrive at the *equivalent* mode I SIF,

$$K_{\mathrm{I,equiv}} = K_{\mathrm{I}} \cos^3(\theta/2) - \tfrac{3}{2} K_{\mathrm{II}} \cos(\theta/2) \sin\theta \tag{17}$$

The energy release rate of a stationary crack, $G(0)$, is expressed in terms of the equivalent mode I SIF and the unmodified mode III SIF by

$$G(0) = \frac{K_{\mathrm{I,equiv}}^2}{E^*} + \frac{K_{\mathrm{III}}^2}{2\mu} \tag{18}$$

where μ is the shear modulus.

To summarize, the advance of the crack front at the vertices is in the plane determined by the *normal* and *binormal* vectors, in the direction given by the angle θ, with a speed which depends on the ratio of the critical energy release rate to the current energy release rate; both quantities are determined for a moving crack. The crack advances in a time step only if the crack growth criterion is satisfied. The crack front advance (or displacement) is given by the product of the crack speed and the time increment.

6.3. *Stress intensity factors*

The stress intensity factors are computed from *interaction energy integrals*; see References 65–67. The interaction energy corresponding to mode M per unit length of the crack front may be written for the dynamic case as[27]

$$\mathscr{I}_{\mathrm{int}}^{(M)} = \int_{V_{\mathrm{ED}}} [-(\sigma_{ij}\varepsilon_{ij}^{(M)} + \rho \dot{u}_i \dot{u}_i^{(M)}) q_{,1} + (\sigma_{ij}^{(M)} u_{i,1} + \sigma_{ij} u_{i,1}^{(M)}) q_{,j} + \rho(\ddot{u}_i^{(M)} u_{i,1} + \ddot{u}_i u_{i,1}^{(M)} - \dot{u}_i^{(M)} \dot{u}_{i,1} - \dot{u}_i \dot{u}_{i,1}^{(M)}) q] \, \mathrm{d}V \Big/ \int_F q \, \mathrm{d}s \tag{19}$$

Here V_{ED} is the volume in which the virtual extension domain, q is an arbitrary function which is positive over the domain V_{ED} but vanishes on the boundary, F is the crack front, and σ_{ij}, ε_{ij}, and u_i are the stresses, strains, and displacements; the quantities superscripted with (M) are the asymptotic fields. We have assumed that to a first approximation the interaction energy is constant within the domain used for the interaction integral, hence the scaling by the line integral $\int_F q \, \mathrm{d}s$ in equation (19). We do not include crack face tractions in equation (19).

The SIFs are related to the interaction energy through

$$K_M = \frac{E^*}{2} \mathscr{I}_{\mathrm{int}}^{(M)} \quad \text{for } M = \mathrm{I}, \mathrm{II} \tag{20}$$

where

$$K_{\mathrm{III}} = \mu \mathscr{I}_{\mathrm{int}}^{(\mathrm{III})} \tag{21}$$

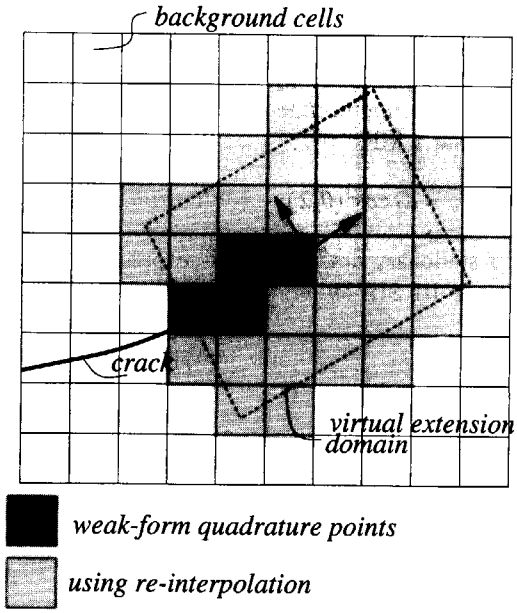

Figure 17. Integration scheme for the interaction energy

6.4. *Asymptotic fields*

The asymptotic displacement and stress fields for a stationary crack are well-known from linear elastic fracture mechanics.[58] We neglect the effects of the crack front curvature on the stress intensity factors. As has been pointed out by Gosz *et al.*,[67] curvature effects can result in non-negligible changes in the computed SIFs.

6.5. *Interaction integral implementation*

To evaluate the integrals of equation (19), a virtual extension domain V_{ED} needs to be established around the crack front. The usual approach in the finite element method is to define the virtual extension domain as a union of finite elements near the crack front.[67] An alternative approach is to define the virtual extension domain as a rectangular box in the local coordinate system of the crack front vertex. Since the integration cells in EFG are independent of the crack surface, we prefer the latter. The question is then, how to integrate equation (19) without having to evaluate the EFG shape functions at a large number of integration points (while the required number of shape function evaluations would pose no problems for the FEM, it would be costly for the EFG method). At the same time we want to make the evaluation sufficiently accurate when the virtual extension domain and the integration cells are misaligned.

Figure 17 shows an arrangement of background cells, a crack, and a virtual extension domain. The $2 \times 2 \times 2$ Gaussian rule we use to evaluate the weak-form integrals in the background cells is not fine enough for cells only partially covering the virtual extension domain. Therefore, we interpolate the primary and derived mechanical fields by the tri-linear shape functions of the hexahedral cells, subdivide each cell into $4 \times 4 \times 4$ subcells, and integrate on these subcells with

a $4 \times 4 \times 4$ Gaussian rule using the interpolated fields. The cost of the trilinear interpolation is relatively low, and the accuracy gained (4096 integration points per cell, instead of only 8) is satisfactory.

However, the trilinear interpolation is not possible for background cells intersected by the crack. Therefore, on these cells we use only the weak-form quadrature points. This procedure is illustrated in Figure 17. The filled cells are those overlapped by the virtual extension domain. There are two types of cells: in the darker cells the interaction integrals are evaluated at the weak-form quadrature points, and in the lighter-colored cells re-interpolation is used.

6.6. *Surface-breaking cracks*

When the crack front breaks a free surface at a right angle, the square root singularity is no longer present, Benthem,[68] and consequently, the energy release rate of equation (10) cannot be based on SIFs. For a crack front not normal to the free surface, no analytical solutions are available, but it has been suggested that the cracks may grow to become inclined with respect to the free surface so as to restore the square root singularity,[69] because that would maximize the energy release rate. Since we cannot deal with these complexities in the present work, we neglect the difference in the order of singularity, and as a temporary expedient we drive the crack at the free surface by the same SIFs as in the interior. However, the computation of the interaction integrals is rather imprecise at the boundary; therefore, we extrapolate the SIFs at the free surface from the closest two interior crack front vertices.

6.7. *Crack effect resolution*

The interaction integrals give good results when the domain of integration is sufficiently large. However, for a surface-breaking crack, the domain needs to be adjusted so that it remains inside the body, and the results for this situation may be inaccurate. An additional difficulty is the loss of resolution when the gap between the crack front and exterior surface is closing.

7. NUMERICAL RESULTS

7.1. *Inclined centre crack in a finite plate*

The first example deals with the determination of Stress Intensity Factors (SIFs) of 3-D cracks. The crack is inclined at 45° in a finite rectangular plate as shown in Figure 18. Tensile tractions $\sigma = 400\,\text{GPa}$ (step function in time) are instantaneously applied at two opposing faces. The material is linear elastic with $E = 200\,000\,\text{GPa}$, $\nu = 0{\cdot}3$ and $\rho = 5000\,\text{kg/m}^3$. Plane strain solutions have been reported by Murti and Valliappan[70] using quarter-point FEM, Dominguez and Gallego[71] using time domain BEM, Fedelinski *et al.*[72]

We have studied the problem as 3-D (the depth of the plate being set to 10) with a grid of $21 \times 37 \times 9$ cells: 3780 hexahedral finite elements and an EFG model with 3213 background cells. The support size is $1{\cdot}25\sqrt{3}h$, where h is the length of the longest edge of the background cell. The results are summarized in Figure 19; they can be seen to be in good agreement with the solution by Dominguez and Gallego,[71] and in even better agreement with the more recent numerical results of Fedelinski *et al.*[72]

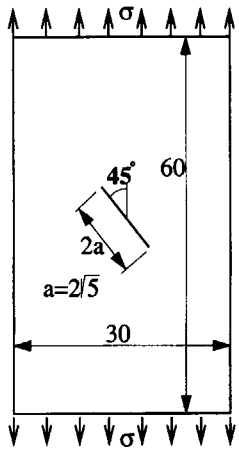

Figure 18. Inclined centre crack in a finite plate under a tensile load

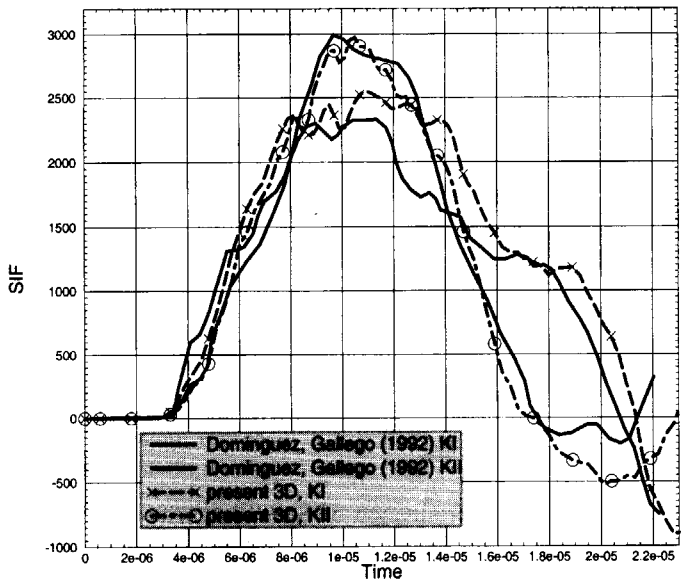

Figure 19. Inclined centre crack in a finite plate under a tensile load. Stress intensity factors of a stationary crack

Next, the crack was grown dynamically. The fracture toughness is 300 GPa$\sqrt{m}$. Figure 20 shows the initial crack and the final crack. Figure 21 depicts the triangulation of the final crack surface. The crack grows almost uniformly, although the growth is a little slower near the free surfaces. A slight amount of roughness develops. This is probably due to the complicated pattern of waves which develops.

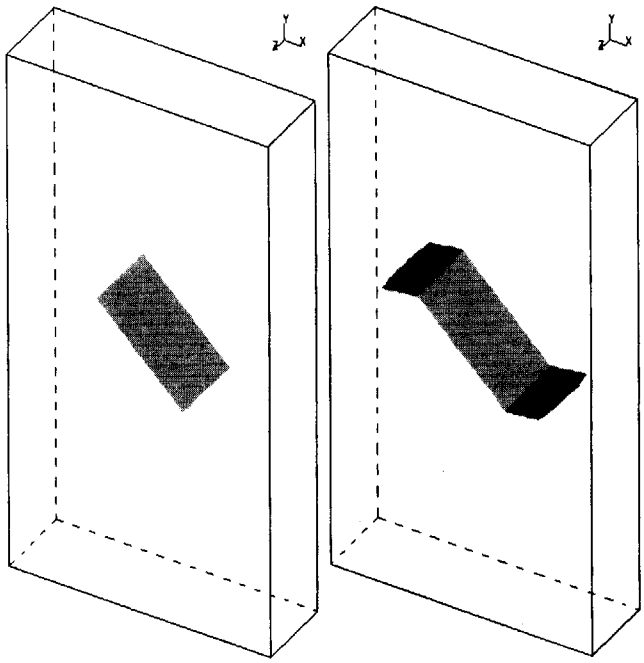

Figure 20. Inclined centre crack in a finite plate: the initial and final stage of crack propagation

7.2. *Centre penny-shaped crack in a finite solid*

The analytical solution for a mode-I penny-shape crack in an infinite medium loaded by a static traction σ at infinity is

$$K_I = 2\sigma\sqrt{\frac{a}{\pi}} \tag{22}$$

where a is the radius of the crack. A crack in a finite cylinder was studied by Jia *et al.*[73] by a singular element BEM technique.

We consider here a penny-shaped crack in a cube. The ratio of the diameter of the initial crack D and the cube edge length w is $D/w = 0{\cdot}3$. We investigate two cases: (i) a stationary crack with a quasi-static loading, and (ii) a propagating crack with a step load. The discretization, consisting of 1350 hexahedral finite elements and 1536 EFG nodes, is shown in Figure 22.

The total number of degrees of freedom was 9216, of which 3072 were internal to the EFG superelement. The cube is 20 m × 20 m × 20 m and the radius of the crack is 2 m.

First, to assess the accuracy achievable with the EFG model, we compute the distribution of the mode-I SIF for a quasi-static loading. We compare with the analytical solution, equation (22), and with the solution of Fedelinski *et al.*[73] for a finite cylinder with the ratio $D/r \approx 0{\cdot}3$ (r is the cylinder radius, $2r = w$), which yields mode-I SIF approximately 2 per cent higher than equation (22). The comparison is shown in Figure 23 and is quite good.

The main goal of this simulation is to demonstrate the ability of the crack representation to model a surface breaking crack. The same material properties and fracture toughness as in Example 7.2

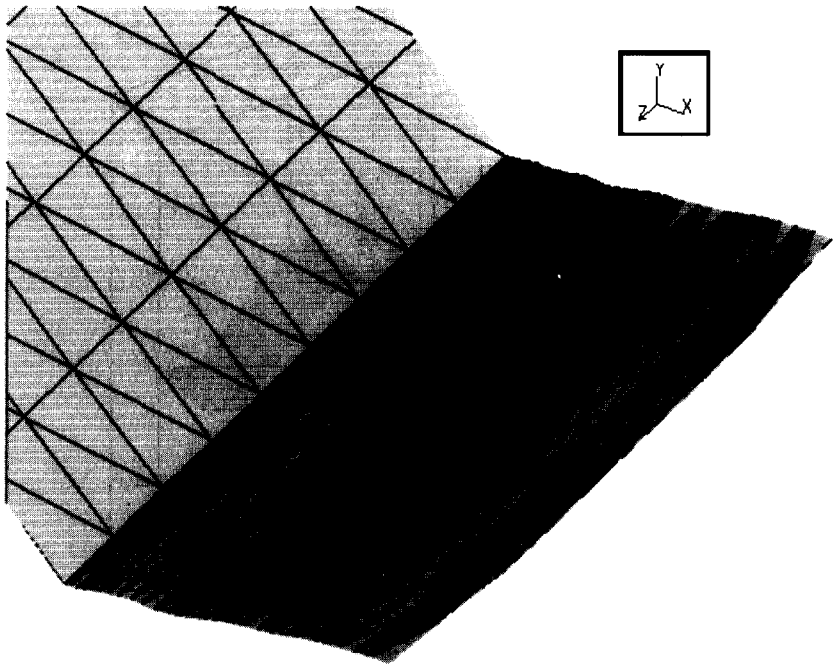

Figure 21. Inclined centre crack in a finite plate: crack surface discretization for the final crack shape

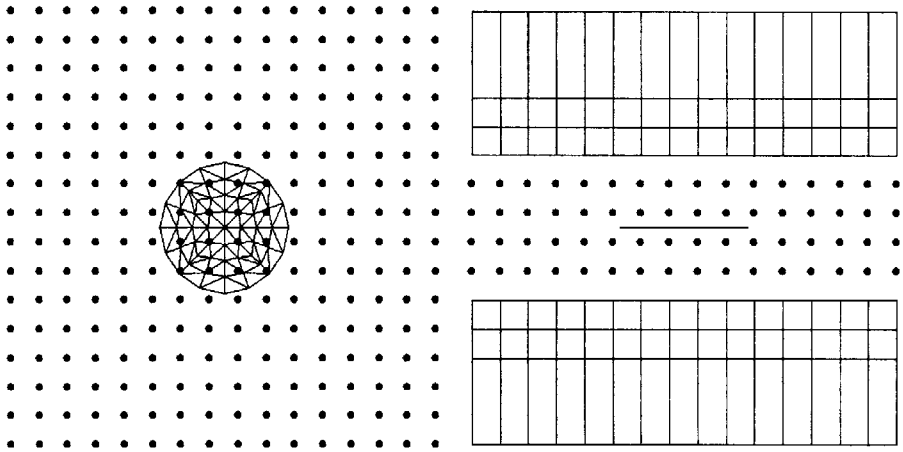

(a) top view (b) front view

Figure 22. Grid for the penny-shaped crack under remote tension

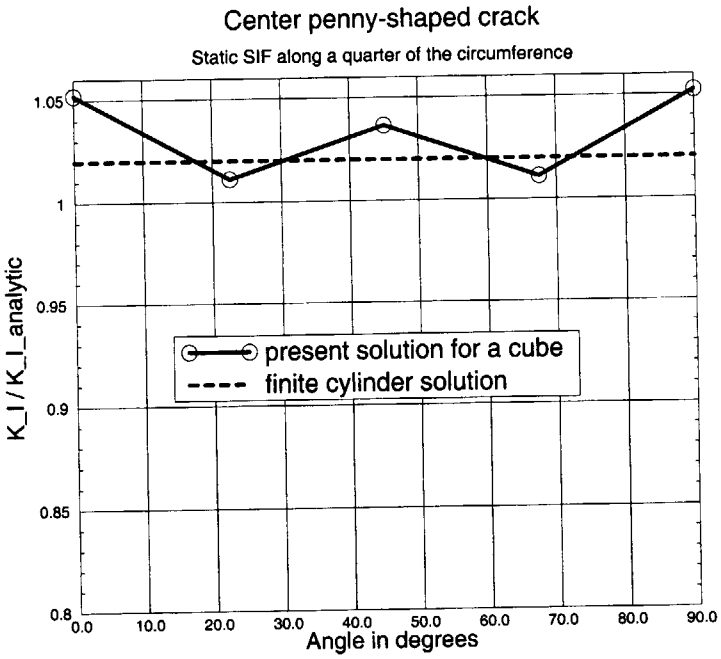

Figure 23. Centre penny-shaped stationary crack. Stress intensity factor along the circumference normalized by the analytic value for an infinite medium

were used. Tensile tractions of 144 GPa are applied as step functions in time at both ends. As can be seen from Figure 24, the crack propagates internally until it reaches the free surfaces of the cube faces. Then the crack front advances to the corners, and severes the cube completely. Figure 24 shows eight stages at equally spaced time intervals (the process takes approximately 2×10^{-5} s for complete separation).

7.3. *Inclined penny-shaped crack*

We consider a penny-shaped crack of radius a which is loaded by a remote uniaxial tension σ, inclined at angle ω with respect to the plane of the crack. The analytic expressions for the stress intensity factors of a crack in an infinite domain are[74]

$$\begin{aligned} K_{\mathrm{I}} &= 2\sigma \sin^2 \omega \sqrt{\frac{a}{\pi}} \\ K_{\mathrm{II}} &= \frac{4\sigma}{(2-\nu)} \sin \omega \cos \omega \sqrt{\frac{a}{\pi}} \sin \theta \\ K_{\mathrm{III}} &= \frac{4(1-\nu)\sigma}{(2-\nu)} \sin \omega \cos \omega \sqrt{\frac{a}{\pi}} \cos \theta \end{aligned} \tag{23}$$

The angles are defined in Figure 25. Numerical solutions for this problem have been presented in Nikishkov and Atluri,[75] Jia *et al.*,[73] Xu and Ortiz,[35] and Young.[76]

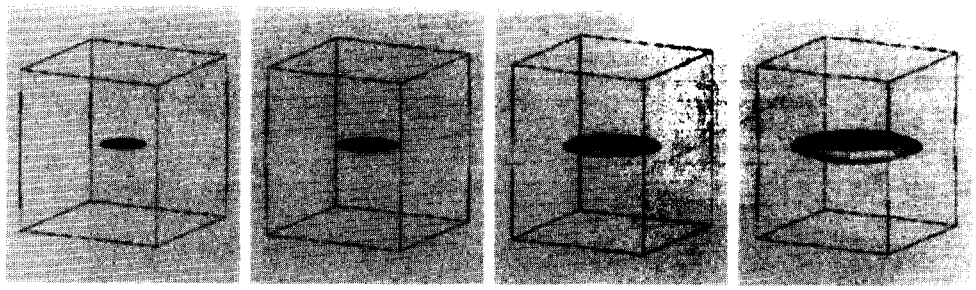

(a) Snapshot 10 (b) Snapshot 20 (c) Snapshot 30 (d) Snapshot 40

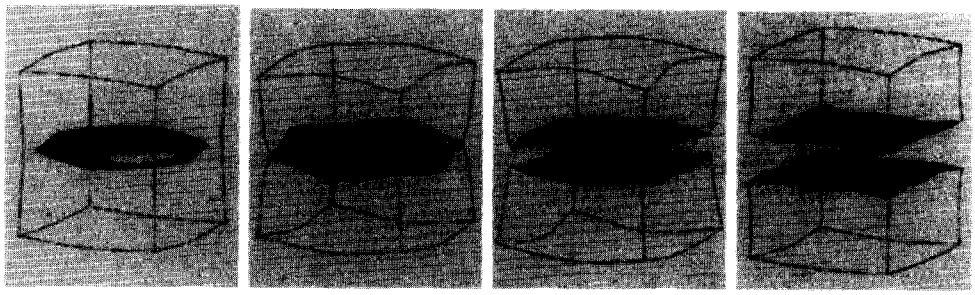

(e) Snapshot 50 (f) Snapshot 60 (g) Snapshot 70 (h) Snapshot 80

Figure 24. Snapshots from the propagation of the centre penny-shaped crack

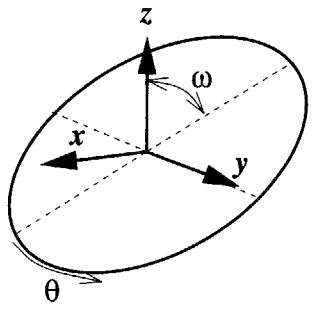

Figure 25. Inclined penny-shaped crack under tension

We consider a finite solid. As shown by Jia *et al.*,[73] the difference between the solution for the unbounded domain and for the finite solid of dimension R is negligible for $a/R \approx 1/10$, and small for $a/R \approx 1/5$. We solve for the stress intensity factor in a cube of side length 20, with a penny-shaped crack inclined by $\omega = 60°$ from the vertical of radius $a = 2$ under a uniform tension applied to opposite faces of the cube. The solution was obtained via explicit dynamic program by increasing the load slowly and using a mass-proportional damping to remove the kinetic energy from the system. The simulation was run until the oscillations in the SIFs were negligible.

The model consists of $34 \times 34 \times 34$ uniformly spaced nodes. The coupled FE/EFG discrete model contained 27812 hexahedral finite elements and an EFG superelement with 8125 background cells.

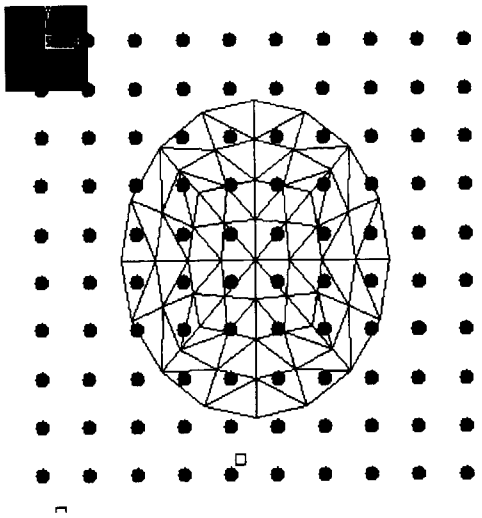

Figure 26. Initial discretization of the crack surface and distribution of EFG nodes around the crack

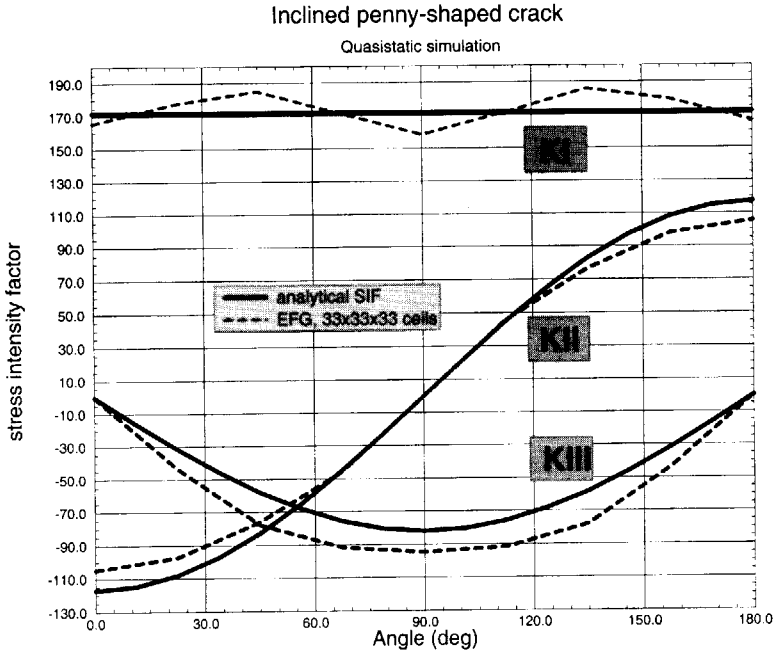

Figure 27. Stress intensity factors of a stationary crack

The support size was set to $1{\cdot}25\times\sqrt{3}h$ (h is the cell size). The results are summarized in Figure 27. While better results have been reported in the literature, it is essential to note that the nodes were uniformly spaced and did not even respect the circular shape of the crack front. In view of this, the resulting accuracy of the SIFs is acceptable.

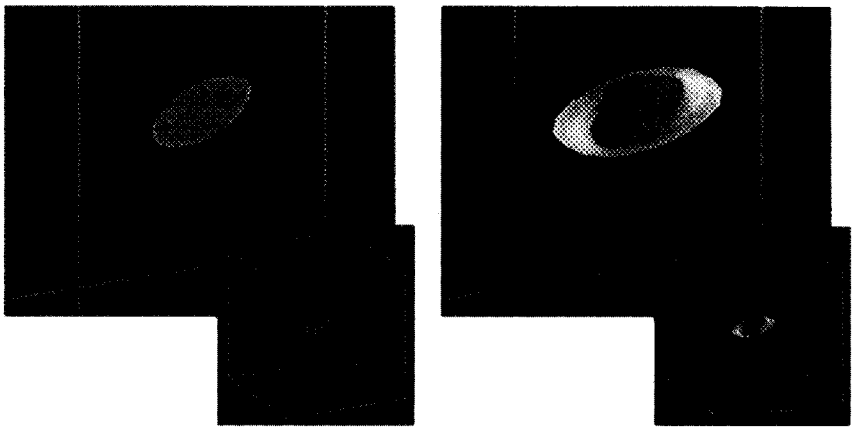

(a) Time $t = 2.0 \times 10^{-6}$ (b) Time $t = 2.94 \times 10^{-6}$

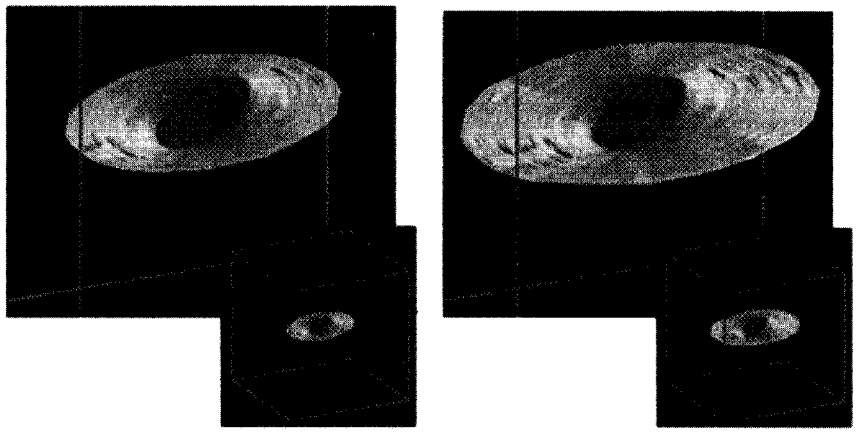

(c) Time $t = 3.88 \times 10^{-6}$ (d) Time $t = 4.82 \times 10^{-6}$

Figure 28. Snapshots from the propagation of the inclined penny-shaped crack

The same model was used to model the dynamic propagation of the crack under tensile load. Tensile tractions of magnitude 144 GPa are applied on the horizontal faces of the cube as step loads. The crack starts propagating at $t = 1{\cdot}92 \times 10^{-6}$. The same material properties as in Example 7.2 were used. Figure 28 shows four snapshots of the propagating crack.

7.4. Through-crack under combined torsion and tension

This example concerns the evolution of a planar centre crack in a rectangular bar loaded by combined tensile force and torsion, see Figure 29. The authors are not aware of any previous numerical solution. The problem illustrates the ability of the present method to model complex three-dimensional crack shapes.

The applied force and torque are step functions in time. The same material properties as in Example 7.2 were used. Figure 2 depicts the discretization. The middle third on the bar was

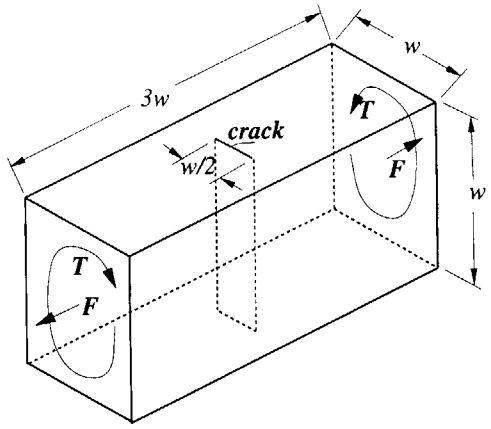

Figure 29. Through-crack under combined torsion and tension. Loading and dimensions

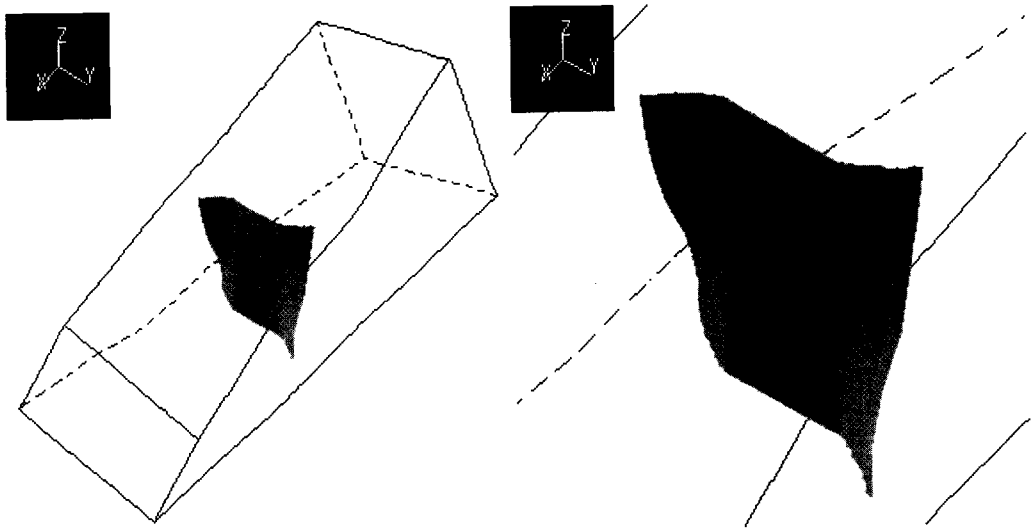

Figure 30. Centre crack in a rectangular bar. Final crack shape: (a) overall view of the deformed bar; (b) closeup of the crack surface

discretized as an EFG superelement, with $18 \times 18 \times 18$ nodes, and the rest with finite elements. Figure 2 also shows the triangulation of the crack surface in the final stage of the crack growth. Figure 30 shows the final shape of the crack.

8. CONCLUSIONS

We have presented a representational model for the growth of arbitrary three-dimensional cracks in the framework of the EFG method. The proposed crack representation is applicable to

non-interacting cracks. The crack front is piecewise linear; we do not allow for crack surface branching.

By using the EFG method, we were able to avoid remeshing. The update of the discrete model consists of the recomputation of the shape functions near the crack front; the integration cells are not changed. Since the methodology does not need automatic mesh generators, we can dispense with an autonomous solid modeling database required for the operation of automatic meshers.

The present crack surface description is based on a triangulation of the crack surface. The physical evolution model relies on stress intensity factors, which are computed from the interaction energy integrals. The crack is propagated in each time step if a crack growth criterion is satisfied. The crack surface vertices are constrained to remain inside the volume or on the boundary faces of the cracked body.

We have demonstrated the method on a number of examples: simulation of mixed-mode growth of centre-through crack in a finite plate, mode-*I* surface-breaking penny-shaped crack in a cube, penny-shaped crack growing under general mixed-mode conditions, and torsion-tension rectangular bar with centre through crack.

To conclude, we review the potential of this method by comparing it with the finite element method with remeshing. (It seems to be a widely accepted view that the FE method with continuous remeshing is a powerful approach to crack propagation problems.) The EFG method has the following advantages for modeling arbitrary crack growth:

8.1. Simple update of the discrete model

Since the geometry of the crack changes with time, the discrete model needs to be updated for each time increment. This is true for all numerical models. However, the update of the EFG model is less extensive than in the FE method. The change in the approximation functions due to crack growth arises from the changes in the nodal supports, whereas in the FE method a new mesh which is compatible with the new crack surface must be constructed.

Since remeshing in any method should be automatic, there is a need to maintain a description of the cracked body which is independent of the mesh, and incorporates the evolving geometry while satisfying the topology and geometry queries of the mesh generator. This has been discussed by Ingraffea and his collaborators.[3, 7, 41, 4, 6] The technique they propose is based on a non-manifold topologically-based BRep (boundary representation) system, which is integrated with the mesh generators.

An FE system for crack growth requires the availability of three components, the mesh generator (M), the analysis package (S), and the solid modeler (U) (refer to Figure 1). The data structures neded in FE systems, their manipulation operators and the communication of information between cooperating components, require a substantial programming effort. This approach is further complicated by the special demands of meshing in the presence of crack surfaces. Crack surfaces are material entities, which means that a material point whose neighbourhood has been split by a running crack needs to assume two distinct identities, one for each of the crack faces. This distinction needs to be preserved in the solid model, so that the mesh generated from the representational model correctly represents the discontinuity surface. To minimize the cost of remeshing and projections between meshes, the mesh outside the neighbourhood of the crack front should be reused. Therefore, the mesh generator must be able to accept part of the old mesh as input in conjunction with the solid model. Another complicating factor in remeshing is that the FE method usually requires the elements to be of a certain shape (e.g. hexahedra) and well-shaped in order

to have good approximating properties. Furthermore, if an embedded singularity is desired in the crack front finite elements, it is necessary to mesh the immediate neighborhood of the front with a special arrangement of elements.[18, 17]

8.2. *Approximation properties of EFG solutions*

Numerical studies show that the EFG method can yield solutions of better accuracy for the same number of degrees of freedom than the FE method. Thus, it becomes possible to avoid the need for excessive refinement near the crack front.

The quadrature cells in the EFG method are independent of the positions of the nodes. Therefore, the numerical integrations of the Galerkin weak form uses the same integration points throughout the simulation. We disregard the effects of the crack in numerical integration of the weak form. This is not possible for the FE method, because when an element is intersected by a crack the element is also used for the construction of the approximation.

To summarize, in the present approach we avoid remeshing of the numerical model in the usual FEM sense. With the moving least-squares construction of the EFG shape functions we can recompute the shape functions without recourse to a mesh generator. Therefore, a topology and geometry representation independent of the mesh is also eliminated. This makes it possible to implement the functionality of a crack propagation modeling system in a single component, working with simple data structures.

ACKNOWLEDGEMENTS

The support of the Office of Naval Research is gratefully acknowledged. We thank John Dolbow and Milan Jirásek for their helpful comments on early versions of the paper.

REFERENCES

1. T. Belytschko, Y. Krongauz, D. Organ, M. Fleming and P. Krysl, 'Meshless methods: An overview and recent developments', *Comput. Meth. Appl. Mech. Engng.*, **139**, 3–47 (1996).
2. L. F. Martha, Topological and geometrical modelling approach to numerical discretization and arbitrary fracture simulation in three dimensions, *Ph.D. Thesis*, Cornell University, Ithaca, New York, 1989.
3. L. F. Martha, P. A. Wawrzynek and A. R. Ingraffea, 'Arbitrary crack representation using solid modeling', *Engng. Computers*, **9**, 63–82 (1993).
4. D. Potyondy, P. Wawrzynek and A. Ingraffea, 'Discrete crack growth analysis methodology for through cracks in pressurized fuselage structures', *Int. J. Numer. Meth. Engng.*, **38**, 1611–1633 (1995).
5. J. Desroches and B. J. Carter, '3 dimensional modelling of a hydraulic fracture', in Mitri Aubertin and Hassani (eds), *Rock Mechanics Tools and Techniques, 2nd North American Rock Mechanics Symposium*, Montreal, Canada, Balkema, Rotterdam, 1996, pp. 995–1002.
6. B. J. Carter, C.-S. Chen, A. R. Ingraffea and P. A. Wawrzynek, 'A topology based system for modeling 3d crack growth in solid and shell structures', in *Proc. 9th Int. Congr. on Fracture*, Sydney, Australia, Elsevier Science Publishers, Amsterdam, 1997.
7. P. A. Wawrzynek, B. J. Carter, A. R. Ingraffea and D. O. Potyondy, 'A topological approach to modeling arbitrary crack propagation in 3d', In G. Kusters and M. Hendriks (eds.), *Proc. 1st Int. DIANA Conf. on Computational Mechanics*, Delft, The Netherlands, 1994, pp. 69–84.
8. T. Nishioka, 'The state of the art in computational dynamic fracture mechanics', *JSME Int. J. Ser. A*, **37**, 313–333 (1994).
9. Y. M. Chen and M. L. Wilkins, 'Numerical analysis of dynamic crack problems', in G. C. Sih (ed.), *Elastodynamic Crack Problems*, Noordhoff, Leiden, 1977.

10. S. Aoki, K. Kishimoto and M. Sakata, 'Finite element computation of dynamic stress intensity factor for a rapidly propagating crack using $\hat{J}$-integral', *Comput. Mech.*, **2,** 54–62 (1987).
11. A. Ivankovic and J. G. Williams, 'The finite volume analysis of linear elastic dynamic fracture', in M. H. Aliabadi (ed.), *Dynamic Fracture Mechanics*, Southampton, UK and Boston, USA, Computational Mechanics Publications, 1995, pp. 101–136.
12. S. N. Atluri and T. Nishioka, 'Numerical studies in dynamic fracture mechanics', *Int. J. Fracture*, **27,** 245–261 (1985).
13. H. M. Koh, H.-S. Lee and R. B. Haber, 'Dynamic crack propagation analysis using Eulerian-Lagrangian kinematic description', *Comput. Mech.*, **3,** 141–155 (1988).
14. R. Gallego and J. Dominguez, 'Dynamic crack propagation analysis by moving singular boundary elements', *J. Appl. Mech. Trans. ASME*, **59,** S158–S162 (1992).
15. H. M. Koh, H. S. Lee and U. Y. Jeong, 'An incremental formulation of the moving grid finite element method for the prediction of dynamic crack propagation', *Nucl. Engng. Des.*, **158,** 295–309 (1995).
16. D. V. Swenson and A. R. Ingraffea, 'Modeling mixed-mode dynamic crack propagation using finite elements: theory and applications', *Comput. Mech.*, **3,** 381–397 (1988).
17. T. N. Bittencourt, P. A. Wawrzynek and A. R. Ingraffea, 'Quasi-automatic simulation of crack propagation for 2-D LEFM problems', *Engng. Fracture Mech.*, **55,** 321–334 (1996).
18. M. Xie, W. H. Gerstle and P. Rahulkumar, 'Energy-based automatic mixed-mode crack propagation modeling', *ASCE J. Engng. Mech.*, **121,** 914–923 (1995).
19. M. Xie and W. H. Gerstle, 'Energy-based cohesive crack propagation modeling', *ASCE J. Engng. Mech.*, **121,** 1349–1358 (1995).
20. A. Portela, M. H. Aliabadi and D. P. Rooke, 'Dual boundary element incremental analysis of crack propagation', *Comput. Struct.*, **46,** 237–247 (1993).
21. Y. Y. Lu, T. Belytschko and L. Gu, 'A new implementation of the element free Galerkin method', *Comput. Meth. Appl. Mech. Engng.*, **113,** 397–414 (1994).
22. T. Belytschko, L. Gu and Y. Y. Lu, 'Fracture and crack growth by element-free Galerkin methods', *Modelling Simul. Mater. Sci. Engng.*, **2,** 519–534 (1994).
23. T. Belytschko, Y. Y. Lu, L. Gu and M. Tabbara, 'Element-free Galerkin methods for static and dynamic fracture', *Int. J. Solids Struct.*, **17/18,** 2547–2570 (1995).
24. T. Belytschko, D. Organ and M. Tabbara, 'Numerical solutions of mixed mode dynamic fracture in concrete using the element-free Galerkin method', in *ICES Conf. Proc.*, 1995.
25. Y. Y. Lu, T. Belytschko and M. Tabbara, 'Element-free Galerkin methods for wave propagation and dynamic fracture', *Comput. Meth. Appl. Mech. Engng.*, **126,** 131–153 (1995).
26. T. Belytschko and M. Tabbara, 'Dynamic fracture using element-free Galerkin methods', *Int. J. Numer. Meth. Engng.*, **39,** 923–938 (1996).
27. D. Organ, Numerical solutions to dynamic fracture problems using the element-free Galerkin method, *Ph.D. thesis*, Northwestern University, 1996.
28. M. Fleming, Y. A. Chu, B. Moran and T. Belytschko, 'Enriched element-free Galerkin methods for crack tip fields', *Int. J. Numer. Meth. Engng.*, **40,** 1483–1504 (1997).
29. J.-P. Ponthot and T. Belytschko, 'Arbitrary Lagrangian Eulerian formulation for element-free Galerkin method', *Comput. Meth. Appl. Mech. Engng.*, submitted.
30. N. Sukumar, B. Moran, T. Black and T. Belytschko, 'An element-free Galerkin method for three-dimensional fracture mechanics', *Comput. Mech.*, (1997) to be published.
31. W. H. Gerstle, L. Martha and A. R. Ingraffea, 'Boundary element modeling of crack propagation in three dimensions', *Engng. Comput.*, **2,** 167–183 (1987).
32. W. H. Gerstle, A. R. Ingraffea and R. Perucchio, 'Three-dimensional fatigue crack propagation analysis using the boundary element method', *Int. J. Fatigue*, **10,** 187–192 (1988).
33. L. N. Germanovich, L. M. Ring, B. J. Carter, A. R. Ingraffea, A. V. Dyskin and K. B. Ustinov, 'Simulation of crack growth and interaction in compression', in Mitri Aubertin, Hassani (ed.), *8th Int. Congr. Rock Mechanics*, Tokyo, Japan, Rotterdam and Brookfield, Balkema, 1996, pp. 219–226.
34. A. F. Bower and M. Ortiz, 'A three-dimensional analysis of crack trapping and bridging by tough particles', *J. Mech. Phys. Solids*, **39,** 815 (1991).
35. G. Xu and M. Ortiz, 'A variational boundary integral method for the analysis of 3D cracks of arbitrary geometry modelled as continuous distributions of dislocation loops', *Int. J. Numer. Meth. Engng.*, **36,** 3675–3701 (1993).
36. G. Xu, F. P. Bower and M. Ortiz, 'An analysis of non-planar crack growth under mixed mode loading', *Int. J. Solids Struct.*, **31,** 2167–2193 (1994).
37. M. Ortiz, 'Computational micromechanics', *Comput. Mech.*, **18,** 321–338 (1996).
38. Y. Mi and M. H. Aliabadi, 'Three-dimensional crack growth simulation using BEM', *Comput. Struct.*, **52,** 871–878 (1994).
39. J. Červenka, Discrete crack modeling in concrete structures, *Ph.D. thesis*, University of Colorado, 1994.
40. P. H. Geubelle and J. R. Rice, 'A spectral method for three-dimensional elastodynamic fracture problems', *J. Mech. Phys. Solids*, **43,** 1791–1824 (1995).

41. B. J. Carter, A. R. Ingraffea and T. N. Bittencourt, 'Topology-controlled modeling of linear and non-linear 3d-crack propagation in geomaterials', in G. Baker and B. Karihaloo (eds.), *Fracture of Brittle Disordered Materials: Concrete, Rock and Ceramics*, E&FN Spon Publishers, Brisbane, Australia, 1995, pp. 301–318.
42. R. Galdos, 'A finite element technique to simulate the stable shape evolution of planar cracks with an application to a semi-elliptical surface crack in a bimaterial finite solid', *Int. J. Numer. Meth Engng.*, **40,** 905–917 (1997).
43. W. S. Cleveland, *Visualizing Data*. AT&T Bell Laboratories, Murray Hill, NJ, 1993.
44. P. Lancaster and K. Salkauskas, *Curve and Surface Fitting: An Introduction*, Academic Press, London, Orlando, 1986.
45. T. Belytschko, Y. Krongauz, M. Fleming, D. Organ and W. K. Liu. 'Smoothing and accelerated computations in the element-free Galerkin method', *J. Comput. Appl. Math.*, to appear.
46. W. K. Liu, S. Jun and Y. F. Zhang, 'Reproducing kernel particle methods', *Int. J. Numer. Meth. Engng.*, **20,** 1081–1106 (1995).
47. P. Krysl and T. Belytschko, 'ESFLIB: A library to compute the element free Galerkin shape functions', *Comput. Meth. Appl. Mech. Engng.*, accepted (1997).
48. T. Belytschko, Y. Krongauz, M. Fleming, D. Organ and W. K. Liu, 'Smoothing and accelerated computations in the element-free Galerkin method', *J. Comput. Appl. Math.*, **74,** 111–126 (1996).
49. P. Krysl and T. Belytschko, 'Element-free Galerkin method: Convergence of the continuous and discontinuous shape functions', *Comput. Meth. Appl. Mech. and Engng.*, **148,** 257–277 (1997).
50. T. Belytschko, D. Organ and Y. Krongauz, 'A coupled finite element–element-free Galerkin method', *Comput. Mech.*, **17,** 186–195 (1995).
51. Y. Krongauz and T. Belytschko, 'Enforcement of essential boundary conditions in meshless approximations using finite elements', *Comput. Meth. Appl. Mech. Engng.*, to appear (1995).
52. T. Belytschko, P. Krysl and Y. Krongauz, 'A three-dimensional explicit element-free Galerkin method', *Int. J. Numer. Meth. Fluids*, **24,** 1253–1270 (1997).
53. P. Krysl and T. Belytschko, 'Object-oriented parallelization of explicit structural dynamics with PVM', *Comput. Struct.*, (1997), accepted.
54. T. Belytschko, Y. Y. Lu and L. Gu, 'Element-free Galerkin methods', *Int. J. Numer. Meth. Engng.*, **37,** 229–256 (1994).
55. J. C. Simo, N. Tarnow and K. K. Wong, 'Exact energy-momentum conserving algorithms and symplectic schemes for nonlinear dynamics', *Comput. Meth. Appl. Mech. Engng.*, **100,** 63–116 (1992).
56. M. Fleming, The element-free Galerkin method for fatigue and quasi-static fracture, *Ph.D. thesis*, Northwestern University, 1997.
57. L. B. Freund, *Dynamic Fracture Mechanics*, Cambridge University Press, Cambridge, 1990.
58. M. F. Kanninen and C. H. Popelar, *Advanced Fracture Mechanics*, Oxford University Press, New York, 1985.
59. J. Hodgdon and J. P. Sethna, 'Beyond the principle of local symmetry: derivation of a general crack propagation law', *Phys. Rev. B*, **47,** 4831 (1993).
60. F. Erdogan and G. C. Sih, 'On the crack extension in plates under plane loading and transverse shear', *J. Basic Engng.*, **85,** 519–527 (1963).
61. M. A. Hussain, S. L. Pu and J. H. Underwood, 'Strain energy release rate for a crack under combined mode *I* and mode *II*', *ASTM*, STP **560,** 2–28 (1974).
62. G. C. Sih, *Mechanics of Fracture Initiation and Propagation: Surface and Volume Energy Density Applied as Failure Criterion*, Kluwer Academic Publishers, Dordrecht, 1991.
63. B. Moran and C. F. Shih, 'Crack tip and associated domain integrals from momentum and energy balance', *Engng. Fract. Mech.*, **27**(6), 615–641 (1987).
64. G. P. Cherepanov, *Mechanics of Brittle Fracture*, McGraw-Hill, New York, 1979.
65. J. F. Yau, S. S. Wang and H. T. Corten, 'A mixed-mode crack analysis of isotropic solids using conservation laws of elasticity', *J. Appl. Mech.*, **47,** 335–341 (1980).
66. C. F. Shih and R. J. Asaro, 'Elastic–plastic analysis of crack on bimaterial interfaces: Part I-small scale yielding', *J. Appl. Mech.*, **55,** 299–316 (1988).
67. M. R. Gosz, J. E. Dolbow and B. Moran, 'An interaction integral formulation for computing stress intensiry factors along curved bimaterial interface cracks', *Int. J. Solids Struct.* (1996), to appear.
68. J. P. Benthem, 'State of stress at the vertex of a quarter-infinite crack in a half-space', *Int. J. Solids Struct.*, **13,** 479–492 (1977).
69. D. A. Hills, P. A. Kelly, D. N. Dai and A. M. Korsunsky, *Solution of Crack Problems: The Distributed Dislocation Technique*, Kluwer Academic Publishers, Dordrecht, Boston, London, 1996.
70. V. Murti and S. Valliappan, 'The use of quarter point element in dynamic crack analysis', *Engng. Fract. Mech.*, **23**(3), 585–614 (1986).
71. J. Dominguez and R. Gallego, 'Time domain boundary element method for dynamic stress intensity factor computations', *Int. J. Numer. Meth. Engng.*, **33,** 635–647 (1992).
72. P. Fedelinski, M. H. Aliabadi and D. P. Rooke, 'Boundary element formulations for the dynamic analysis of cracked structures', in M. H. Aliabadi (ed.), *Dynamic Fracture Mechanics*, Computational Mechanics Publications, Southampton, UK and Boston, USA, 1995, pp. 61–100.

73. Z. H. Jia, J. Shippy and F. J. Rizzo, 'Three-dimensional crack analysis using singular boundary elements', *Int. J. Numer. Meth. Engng.*, **28,** 2257–2273 (1989).
74. Y. Murakami (ed.), *Stress Intensity Factors Handbook*, Vol. 2, 1 edn, Pergamon Press, New York, 1986.
75. G. P. Nikishkov and S. N. Atluri, 'Calculation of fracture mechanics parameters for an arbitrary three-dimensional crack, by the 'Equivalent Domain Integral' method', *Int. J. Numer. Meth. Engng.*, **24,** 1801–1821 (1987).
76. A. Young, 'A single domain boundary element method for 3d elastostatic crack analysis using continuous elements', *Int. J. Numer. Meth. Engng.*, **39,** 1265–1293 (1996).